ELSEVIER

International Journal of Mass Spectrometry 218 (2002) 37–48

International Journal of Mass Spectrometry

www.elsevier.com/locate/ijms

The dissociation dynamics and thermochemistry of the acrolein ion studied by threshold photoelectron–photoion coincidence spectroscopy

Yue Li, Tomas Baer*

Department of Chemistry, University of North Carolina, Chapel Hill, NC 27599-3290, USA

Received 11 January 2002; accepted 28 March 2002

Abstract

Threshold photoelectron–photoion coincidence spectroscopy has been used to investigate the dissociation dynamics of the acrolein ion ($CH_2CHCHO^{\bullet+}$). The two lowest energy dissociation channels to $C_2H_4^{\bullet+} + CO$ and $C_3H_3O^+ + H^\bullet$ are observed at photon energies between 10.0 and 12.0 eV. The $C_2H_4^{\bullet+}$ ion time-of-flight distributions exhibit characteristics of a two-component reaction rate. A three-well-two-channel model is proposed to explain the multi-component dissociation rate. The simulation that fits both the time-of-flight distributions and the breakdown diagram shows that the slow component of the reaction rate for $C_2H_4^{\bullet+}$ production is dominantly caused by tunneling through the isomerization barrier connecting the acrolein ion (A) and the distonic ion, $^\bullet CH_2CH_2CO^+$ (B). After being produced, only small amounts of B isomerize to the lowest energy conformer, the methylketene ion (C). The energy barrier heights of the isomerization from A to B and the $C_3H_3O^+$ ion production are 0.87 ± 0.02 and 0.92 ± 0.02 eV, respectively. The 0 K appearance energy of the $C_3H_3O^+$ ion is determined to be 11.03 ± 0.02 eV. Using the acrolein heat of formation of -69 ± 10 kJ/mol, the 298 K heat of formation of the CH_2CHCO^+ ion is determined to be 783 ± 10 kJ/mol. (Int J Mass Spectrom 218 (2002) 37–48)

Keywords: Acrolein; TPEPICO; Dissociation; Thermochemistry; Photoionization mass spectra

1. Introduction

The gas phase photochemistry of neutral acrolein (CH_2CHCHO), one of the smallest unsaturated carbonyl compounds, has been well studied [1–3]. It is thus surprising that no photoionization study of the ionic dissociation dynamics has been reported.

The photoelectron spectrum of acrolein has been measured by several groups and the ionization energy (IE) was determined to be 10.11 eV [4–8]. The only information about the fragmentation of the ion has come from some early electron ionization appearance energy (AE) measurements, in which the *m/z* 29 (HCO^+) and *m/z* 27 ($C_2H_3^+$) fragments were reported [9–11]. These two ions correspond to the direct dissociation of the acrolein ion by cleavage of the C–C single bond. More recently, collision-induced dissociation studies of the acrolein ion by Maquestiau et al. [12] and Traeger et al. [13] showed that the acrolein ion at low energies dissociates primarily via $H^\bullet$ atom and CO loss reactions. A similar spectrum was obtained for methylketene. The similarity of the acrolein and methylketene dissociation suggests that these ions isomerize and dissociate via a common

* Corresponding author. E-mail: baer@unc.edu

1387-3806/02/$ – see front matter
PII S1387-3806(02)00644-9

mechanism. McLafferty and coworkers [14,15] studied the formation, isomerization and dissociation of three $C_3H_4O^{\bullet+}$ isomers, acrolein, the distonic ion ($^{\bullet}CH_2CH_2CO^+$) and methylketene ($CH_3CHCO^{\bullet+}$), using the neutralization–reionization mass spectrometry (NRMS). They obtained similar product ions of mass numbers 55 ($C_3H_3O^+$) and 28, 27 and 26 ($C_2H_4^{\bullet+}$, $C_2H_3^+$ and $C_2H_2^{\bullet+}$).

In contrast to the sparse experimental data on the acrolein ion dissociation, a number of theoretical calculations of the $C_3H_4O^{\bullet+}$ isomers have been reported. These are reviewed in the accompanying paper [16].

In this paper, we report the experimental results on the dissociation reactions of the acrolein ion obtained with threshold photoelectron–photoion coincidence (TPEPICO) spectroscopy, a technique by which the molecular ions can be energy-elected. The analysis of the breakdown diagram and the ion time-of-flight distributions provides information about the dissociation dynamics including the dissociation rate constants as well as information about isomerization reactions. Finally, dissociation onsets provide information about the fragment ion heats of formation.

2. Experimental approach

The TPEPICO apparatus has been described in detail previously [17,18]. Briefly, room temperature sample vapor was leaked into the experimental chamber through a 1.0 mm diameter inlet and then was ionized with vacuum ultraviolet (VUV) light from an H_2 discharge lamp dispersed by a 1 m normal incidence monochromator. The VUV wavelengths were calibrated using the hydrogen Lyman-α line. The ions and the electrons were extracted in opposite directions with an electric field of 20 V/cm. Threshold photoelectrons were selected by a recently developed velocity focusing electron analyzer [19]. This analyzer has a threshold electron collection efficiency of 45%, a combined photon and electron energy resolution of about 13 meV, and excellent suppression of energetic (hot) electrons. Ions are accelerated in the first 5 cm long acceleration region to 100 eV and then accelerated to 220 eV in a short second region. The ions were detected after drifting through a 30 cm field-free drift region. The electrons detected by a channeltron electron multiplier and ions detected by a multi-channel plate detector were used as start and stop pulses for measuring the ion time-of-flight (TOF). The TOF for each coincidence event was stored on a multi-channel pulse height analyzer. TOF distributions were obtained in 1–24 h depending on the photon intensity and the desired spectrum quality.

Two types of experiments were carried out. First, the fractional abundances of the parent and the daughter ions were measured as a function of the photon energy (breakdown diagram). Second, the product ion TOF distributions were measured at energies close to the dissociation limit of the parent ion. Slowly dissociating (metastable) ions decay in the first acceleration region. The resulting product ion TOF distribution, which is asymmetrically broadened toward long TOF, can be analyzed to extract the ion dissociation rates as a function of ion internal energy.

The acrolein sample (C_3H_4O, 90%, Aldrich) was used without further purification. The small amounts of water and cyclic acrolein dimer impurities did not affect the analysis of experimental mass spectra.

3. Quantum chemical calculations

In the simulations for the experimental data, reliable vibrational frequencies of the equilibrium structures and the transition states are required to calculate the energy distribution of the molecular ion and reaction rate constants. These were obtained with quantum chemical calculations using Gaussian-98 package [20], discussed in detail in the accompanying paper [16]. Briefly, all neutral and ionic species were fully optimized at the HF/6-31G* and DFT (B3LYP)/6-31G* levels. The stationary points and first-order saddle points were confirmed through the calculation of harmonic vibrational frequencies. The transition states were obtained using the synchronous transit-guided quasi-Newton (STQN) methods [21,22]. For all transition states, the intrinsic reaction coordinate (IRC)

Table 1
Frequencies used in the energy distribution and RRKM calculations

C_3H_4O	175, 320, 572, 612, 929, 993, 1023, 1044, 1181, 1309, 1410, 1475, 1701, 1805, 2901, 3162, 3199, 3251
$C_3H_4O^{\bullet+}$ (A)	200, 325, 492, 591, 888, 951, 955, 1087, 1134, 1206, 1315, 1412, 1498, 1637, 2935, 3179, 3234, 3273
$C_3H_4O^{\bullet+}$ (B)	195, 215, 381, 523, 652, 788, 836, 1022, 1093, 1262, 1268, 1416, 1466, 2306, 3029, 3080, 3199, 3328
$C_3H_4O^{\bullet+}$ (C)	113, 208, 428, 608, 669, 853, 952, 1109, 1151, 1335, 1396, 1438, 1494, 2258, 3002, 3041, 3172, 3188
TS_{AB}	−1060[a], 214, 415, 565, 625, 758, 872, 912, 1066, 1112, 1233, 1397, 1491, 1534, 2194, 3163, 3195, 3310
TS_{BC}	−1378[a], 214, 322, 502, 613, 794, 867, 887, 1088, 1158, 1222, 1396, 1460, 2218, 2285, 3165, 3199, 3331
TS_1	−137[a], 80, 127, 131, 225, 653, 806, 912, 1051, 1211, 1282, 1456, 1533, 2257, 3145, 3153, 3247, 3266
TS_2	−532[a], 79, 330, 380, 539, 603, 708, 890, 928, 1088, 1095, 1299, 1452, 1643, 2219, 3163, 3188, 3286

[a] Reaction coordinate.

calculations were performed to verify the transition states obtained to be the right transition states.

According to calculations [16] of the various $C_3H_4O^{\bullet+}$ ion structures, three low energy isomers are involved in the low energy dissociation of the acrolein ion. These are the acrolein ion (A), $^{\bullet}CH_2CH_2CO^+$ (B) which is a distonic ion produced from acrolein by a 1,2-H atom shift, and the lowest energy methylketene ion, $CH_3CHCO^{\bullet+}$ (C), which is formed from B via another H atom shift. The transition states connecting them are TS_{AB} and TS_{BC}, respectively. The lowest energy dissociation channel to $C_2H_4^{\bullet+} + CO$ proceeds directly from isomer B. However, the acrolein ion needs to overcome an energy barrier (TS_{AB}) to produce B. Once formed, B can either dissociate or isomerize further via TS_{BC} to form the lowest energy structure C. A second dissociation channel to $C_3H_3O^+ + H^{\bullet}$ has a slightly higher calculated onset. Table 1 lists the vibrational frequencies of neutral acrolein, as well as those of ions and transition states. These frequencies are used in the calculations of the thermal energy distribution and dissociation rate constants.

4. Results and discussion

4.1. The TOF distributions and breakdown diagram

The TOF mass spectra were collected in the photon energy range of 10.0–14.0 eV. Typical TOF distributions at low energies, in which the reaction rates constants are small, are shown in Fig. 1. The points correspond to experimental data while the solid lines corresponds to the fitted TOF distributions (as discussed in the following section). The ion peak at about 17.4 μs, assigned to the parent ion, $C_3H_4O^{\bullet+}$ (*m*/*z* 56), consists of two parts, a central peak on top of a broader one. The sharp part results from the effusive

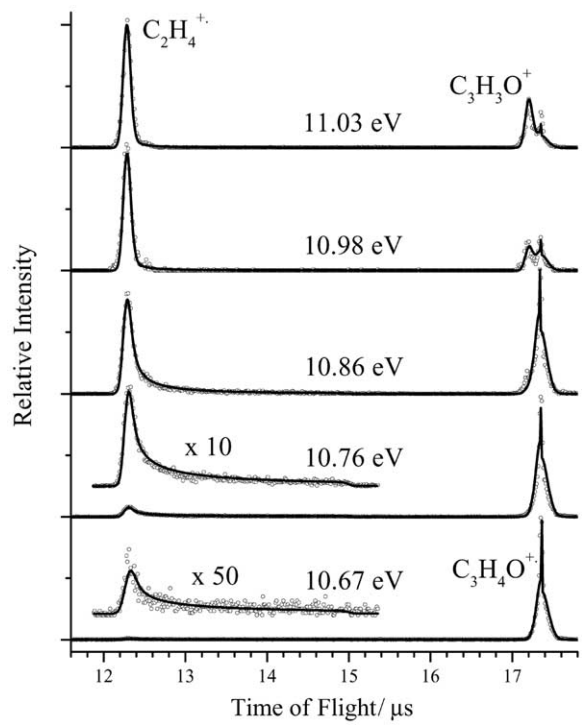

Fig. 1. Ion TOF distributions at different photon energies. The points are the experimental data and the solid lines are the simulation results.

jet produced by the sample inlet, while the broad peak results from the acrolein vapor in the background. The simulation shows that the proportion from the effusive jet is less than 1%. At a photon energy below 10.8 eV, the only product ion is $C_2H_4^{\bullet+}$ (*m*/*z* 28). The $CO^{\bullet+} + C_2H_4$ product channel, which also produces a mass 28 ion, is ruled out on energetic grounds because its thermochemical threshold is some 3.5 eV above that of the $C_2H_4^{\bullet+} + CO$ products. At photon energies in excess of 10.8 eV, a peak at *m*/*z* 55, which corresponds to the $H^{\bullet}$ loss product, $C_3H_3O^+$, appears.

Fig. 2 shows the breakdown diagram of the acrolein ion between 10 and 12 eV. The points are the experimental ratios with error estimates, while the solid lines are the simulation results. As is evident in the TOF mass spectra in Fig. 1, at low energies the $H^{\bullet}$ loss fragment peak (*m*/*z* 55) is not well resolved from the parent ion, and so the peak areas of the fragment ion and the parent ion were determined by fitting the peak shapes with two (for the parent ion) and one (for the fragment ion) Gaussian functions, respectively, to obtain a more accurate breakdown diagram.

Although the breakdown diagram shown in Fig. 2 extends just up to 12 eV, additional fragment ions were observed at higher energies. Their phenomenological onsets (i.e., not modeled in detail) were HCO^+ at 12.7 eV, $C_2H_3^+$ at 13.0 eV, and $C_2H_2^{\bullet+}$ at 13.1 eV. The further analysis to determine thermochemical onsets for HCO^+, $C_2H_3^+$ or $C_2H_2^{\bullet+}$ was not attempted because the peaks of *m*/*z* 26, 27, 28 and 29 are poorly resolved due to broadening as a result of kinetic energy release. The DFT calculated [16] appearance energies of HCO^+, $C_2H_3^+$ and $C_2H_2^{\bullet+}$ are 12.55, 12.94 and 13.27 eV, respectively. A complete analysis would require taking into account the thermal energy of the sample, which shifts the onsets to lower energy, and the kinetic shift, which shifts the onsets to higher energy. Because these two effects shift the onsets in opposite directions [23], the phenomenological onsets already mentioned are within about 0.2 eV of the 0 K onsets, and indeed they agree fairly well with the DFT calculated onsets. The appearance of the $C_2H_2^{\bullet+} + H_2CO$ channel at 13.1 eV is somewhat surprising because according to the DFT calculations, its charge transfer pair, $C_2H_2 + H_2CO^{\bullet+}$, has a

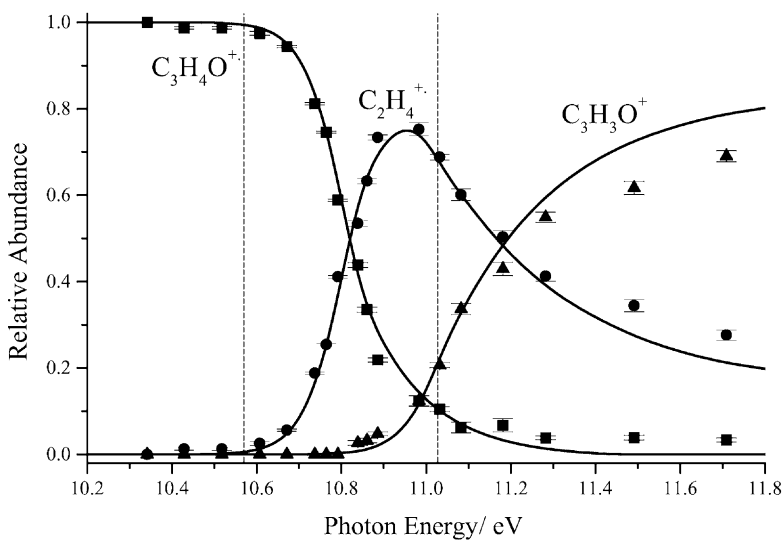

Fig. 2. Breakdown diagram of $C_3H_4O^{\bullet+}$ showing the relative abundance of the precursor and the two fragment ions as a function of the ion internal energy. The points are the experimental data with error estimates, and the solid lines are the simulation results. The dashed lines indicate the derived 0 K dissociation onsets for the $CH_2CHCO^+ + H^{\bullet}$ channel and the thermochemical dissociation onset for the $C_2H_4^{\bullet+} + CO$ products. Our derived upper limit for the latter channel is at 10.76 eV.

thermochemical onset that lies 0.44 eV below 13.1 eV. Yet, we see no evidence for any *m/z* 30 ions.

At low photon energies between 10.6 and 11.0 eV, the peak shapes of the $C_2H_4^{\bullet+}$ ion TOF distributions in Fig. 1 are found to be comprised of two parts, one symmetric Gaussian peak, which corresponds to a fast reaction, and one asymmetric peak tailing toward the parent ion. Asymmetric TOF distributions indicate a slow ion dissociation caused by the production of daughter ions during the course of acceleration. However, two component TOF distributions indicate that some ions dissociate rapidly, while others dissociate slowly.

4.2. The simulation of the experimental data

In order to fit the experimental two-component TOF distributions, a three-well-two-channel model is suggested to describe the dissociation and isomerization reactions of the acrolein ion on the basis of our theoretical results [16]. The two-dimensional depiction of this potential energy surface is shown in Fig. 3. The differential equations associated with the potential energy surface are given by Eq. (1):

$$\frac{d[P_1]}{dt} = k_3[B], \qquad \frac{d[A]}{dt} = -(k_1 + k_6)[A] + k_2[B],$$
$$\frac{d[B]}{dt} = k_1[A] - (k_2 + k_3 + k_4)[B] + k_5[C],$$
$$\frac{d[C]}{dt} = k_4[B] - k_5[C], \qquad \frac{d[P_2]}{dt} = k_6[A] \tag{1}$$

where A, B and C refer to the three isomers of $C_3H_4O^{\bullet+}$, P_1 the $C_2H_4^{\bullet+} + CO$ channel, and P_2 is the $C_3H_3O^+ + H^\bullet$ channel. The DFT calculations [16] indicate that ion C can also dissociate directly to the P_2 channel. However, once the C ion is formed, dissociation to P_1 (CO loss) dominates over the $H^\bullet$ loss channel so that the back reaction can be ignored.

The solutions of the system of equations, obtained with the aid of Mathematica, yield the following results:

$$[A](t) = \alpha_1 \exp(-k_{fast}t) + \alpha_2 \exp(-k_{med}t) + \alpha_3 \exp(-k_{slow}t),$$

$$[B](t) = \frac{(k_1 + k_6 - k_{fast})\alpha_1}{k_2} e^{-k_{fast}t} + \frac{(k_1 + k_6 - k_{med})\alpha_2}{k_2} e^{-k_{med}t} + \frac{(k_1 + k_6 - k_{slow})\alpha_3}{k_2} e^{-k_{slow}t},$$

$$[P_1](t) = \frac{(k_1 + k_6 - k_{fast})k_3\alpha_1}{k_2 k_{fast}}(1 - e^{-k_{fast}t}) + \frac{(k_1 + k_6 - k_{med})k_3\alpha_2}{k_2 k_{med}}(1 - e^{-k_{med}t}) + \frac{(k_1 + k_6 - k_{slow})k_3\alpha_3}{k_2 k_{slow}}(1 - e^{-k_{slow}t}),$$

$$[P_2](t) = \frac{k_6\alpha_1}{k_{fast}}(1 - e^{-k_{fast}t}) + \frac{k_6\alpha_2}{k_{med}}(1 - e^{-k_{med}t}) + \frac{k_6\alpha_3}{k_{slow}}(1 - e^{-k_{slow}t}) \tag{2}$$

where k_{fast}, k_{med} and k_{slow} are the three roots of the following cubic equation:

$$k_i^3 - (k_1 + k_2 + k_3 + k_4 + k_5 + k_6)k_i^2 + [(k_2 + k_3 + k_4)(k_1 + k_6) - k_1k_2 + (k_1 + k_2 + k_3 + k_6)k_5]k_i + [k_1k_2k_5 - (k_2 + k_3)(k_1 + k_6)k_5] = 0 \tag{3}$$

The solution for [C](*t*) is not shown because it is even more complicated than the equations shown. The parameters, α_1, α_2, and α_3 are determined by the initial conditions, such as $[A](t = 0) = 1 = \alpha_1 + \alpha_2 + \alpha_3$, $[B](t = 0) = 0$, and $[C](t = 0) = 0$.

The rate constants in the Eq. (3) can be calculated using the statistical RRKM theory formula [24].

$$k(E) = \frac{\sigma N^{\neq}(E - E_0)}{h\rho(E)} \tag{4}$$

in which E_0 is the activation energy, $N^{\neq}(E - E_0)$ the sum of states of the transition state from 0 to $E - E_0$, $\rho(E)$ the density of states of the ion, respectively, and σ is the symmetry parameter, which is 1 for all the reactions shown in Fig. 3.

Slow dissociation rate constants can be explained by two mechanisms. According to the statistical theory of unimolecular decay, if the activation energy for a dissociation step is large, the rate constant will be slow primarily because the density of vibrational states

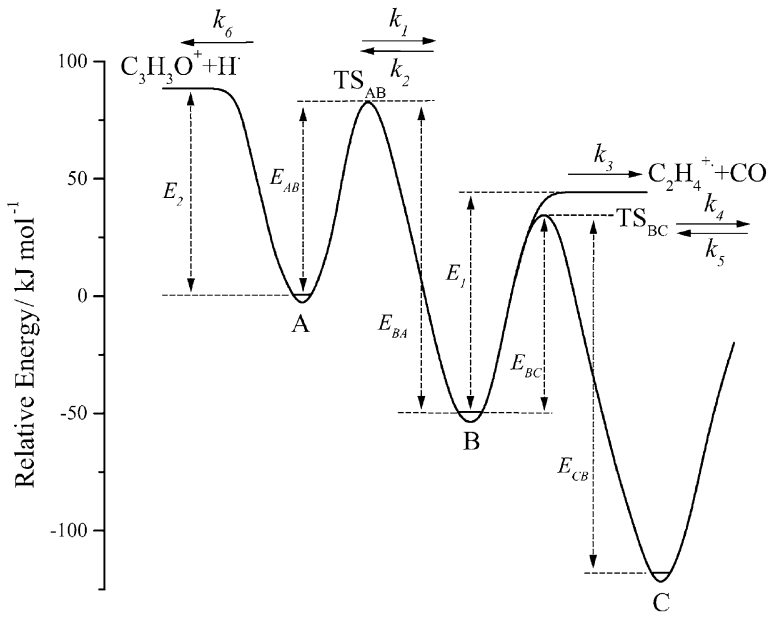

Fig. 3. Three-well-two-channel model of the acrolein dissociation and isomerization reactions.

of the molecular ion is very large. In the dissociation of the acrolein ion, the phenomenological activation energy is not large. Yet, the rate constant at threshold is very slow. This slow rate constant can arise if the acrolein ion were to isomerize into a much lower energy structure prior to dissociation. Previous experiments as well as theoretical calculations (as discussed in Section 1) showed that several isomers are lower in energy than the acrolein ion. In addition, our own calculations (accompanying paper) have shown that at least two of these, the distonic and methylketene ions can be reached by relatively low barriers from the acrolein ion structure.

We thus attempted to fit the breakdown diagram and the asymmetric TOF distributions with a model that involved the rapid isomerization of the acrolein ion into the deep wells associated with the distonic ion and the methylketene ion. Such a model was successful in describing the dissociation dynamics of the pentene isomers [25] as well as a number of small ester ions [26–28]. By adjusting the energies of the various ionic structures and the heat of formation of the acrolein molecule, it was possible to fit the data in Figs. 1 and 2. However, the fit could only be achieved if the measured $C_2H_4^{\bullet+}$ appearance energy was close to thermochemical dissociation limit to $C_2H_4^{\bullet+}+CO$. This requirement meant that the heat of formation of the acrolein molecule would have to be lowered by some 25 kJ/mol below its currently accepted value, a value that has been calculated a number of times by high level ab initio [16,29] and molecular mechanics [30] methods. Thus, we searched for an alternative mechanism to explain the slow rate constant.

A second mechanism that results in a slow rate constant is tunneling through a potential barrier. Thus, even a reaction with a small activation energy can have a slow rate constant [31]. As pointed out in the accompanying paper, the loss of CO from the acrolein ion involves a hydrogen atom transfer, which suggests that tunneling could play an important role. Therefore, the rate constants, k_1, k_2, k_4 and k_5, which correspond to the isomerization processes between A and B or B and C, were calculated using the following RRKM theory formula with the tunneling correction

[24,32]:

$$k(E) = \frac{\sigma}{h\rho(E)} \int_{-E_0}^{E-E_0} \kappa(\varepsilon_t)\rho^{\neq}(E - E_0 - \varepsilon_t)\,\mathrm{d}\varepsilon_t \quad (5)$$

in which $\rho^{\neq}(E)$ is the density of states of the transition state, ε_t is the translational energy in the reaction coordinate, and $\kappa(\varepsilon_t)$ is the tunneling probability modeled with an Eckart barrier [24].

Since the sample used in the experiments is at room temperature, it has a thermal energy distribution. In addition, the electron analyzer function has a width of 13 meV. These broadening features must be taken into account in modeling of the ion TOF distributions and the breakdown diagram.

The internal energy distribution of the neutral sample at 298 K was calculated using the Boltzmann formula:

$$P(E) = \frac{\rho(E)\,\mathrm{e}^{-E/RT}}{\int_0^{\infty} \rho(E)\mathrm{e}^{-E/RT}\,\mathrm{d}E} \quad (6)$$

in which the rovibrational density of states, $\rho(E)$, is calculated using a direct count method [24,33]. The acrolein molecule can be approximated as a symmetric top by replacing the calculated rotational constants (47.96, 4.629 and 4.222 GHz) with the geometric average of the latter two (4.421 GHz). To obtain the ion internal energy distribution, this thermal energy distribution in the neutral acrolein is then convoluted with the electron energy analyzer function that is obtained from a threshold photoelectron spectrum (TPES) of Xe [19].

The ion TOF distributions and the breakdown diagram can be calculated using the following known information: the thermal energy distribution of the molecular ion, the acceleration electric fields, the acceleration and drift distances, and the adiabatic ionization energy of the acrolein, 10.11 ± 0.01 eV [34], a value confirmed in our experiment. In the simulation calculations, we assumed the vibrational frequencies determined from the DFT calculations [16], and varied only the six energies shown in Fig. 3. The initial set of energies, derived from the DFT calculation [16], were 0.86 eV (E_{AB}), 1.35 eV (E_{BA}), 0.94 eV (E_{BC}), 1.54 eV (E_{CB}), 0.99 eV (E_1) and 0.92 eV (E_2). These relative energies for the acrolein, distonic, and methylketene ions are ones that are close to the accepted experimental and theoretical values [29,35,36]. The six energies were then varied in a program that calculated the TOF distributions and the breakdown diagram, and compared them to the experimental data in Figs. 1 and 2 until a best least squares fit was obtained. The TOF distributions at low energies are sensitive to the magnitude of the rate constants, while the breakdown diagram is sensitive only to the ratio of rate constants, but over a wider energy range.

In order to obtain an estimate of the errors associated with the derived energy parameters, the energy barrier heights or the well depths were individually adjusted and held fixed (one at a time), while the rest of the parameters were allowed to vary for an optimum fit. These parameters were varied until the overall fit to the data worsened noticeably. In this manner, it was possible to not only determine the error limits on each parameter, but also determine its effect on the simulation quality.

The simulations indicate that the breakdown diagram is dominantly influenced by E_{AB} and E_2, and is also slightly affected by the $C_2H_4^{\bullet+} + CO$ channel energy relative to the A well (i.e., $E_{AB} - E_{BA} + E_1$). This is because all of the $H^{\bullet}$ loss product is formed directly from the A isomer so that all ions that isomerize to B produce only the CO loss product. Thus, the breakdown diagram is fitted almost exclusively by the ratio of $k_6(E)$ to $k_1(E)$. This fixes the energies, E_2 and E_{AB}. The breakdown diagram is of course also strongly influenced by the entropies of activation of the transition states leading to $H^{\bullet}$ loss and isomerization to B. However, these frequencies are largely fixed by our DFT calculations.

The simulations also show that the depths of the B and C wells and the energy barrier height of TS_{BC} are of little importance for the simulation of the experimental breakdown diagram and TOF distributions within ± 0.30 eV, a value higher than the assumed error limits of the DFT results [16]. Thus, in the simulation, the B ion is fixed at the DFT calculated 0 K thermochemical energy 866 kJ/mol, and the C ion

is fixed at the evaluated value, 799 kJ/mol based on the several experimental and theoretical results [16]. With this greatly simplified simulation, the best fit to the experimental data in Figs. 1 and 2 was obtained with the following set of energies, which are very close to the original DFT values: 0.87 (E_{AB}), 1.40 eV (E_{BA}), 0.89 eV (E_{BC}), 1.59 eV (E_{CB}), 0.99 eV (E_1), and 0.92 eV (E_2). The simulation fixes the values of E_{AB} and E_2 to within ±0.02 eV. Thus, the 0 K thermochemical dissociation limit for $C_3H_3O^+$ formation is determined to be 11.03 ± 0.02 eV. The simulation also determines an upper limit of 0.65 eV for the $C_2H_4^{\bullet+} + CO$ channel energy, ($E_{AB} - E_{BA} + E_1$). When this energy is higher than 0.65 eV, the simulation quality of the breakdown diagram becomes significantly worse. Thus, the upper limit of the $C_2H_4^{\bullet+}$ appearance energy is 10.76 eV. However, this energy is 0.19 eV above the thermochemical value based on the known heats of formation of $C_2H_4^{\bullet+} + CO$, and the calculated heat of formation of the acrolein molecule (discussed in the following section). In other words, it is the TS_{AB} barrier that determines the $C_2H_4^{\bullet+}$ onset energy and not the final product energies.

The RRKM calculated rate constant curves ($k_1 \rightarrow k_6$) using the energies that yielded the best fit are shown in Fig. 4 along with the activation entropies for each channel. These entropies were calculated at 600 K with the ion and transition state frequencies as described by Baer et al. [17]. The rate constants, k_3 and k_6 have positive activation entropies, which indicates that the two reactions proceed via loose transition states. This is consistent with the fact that

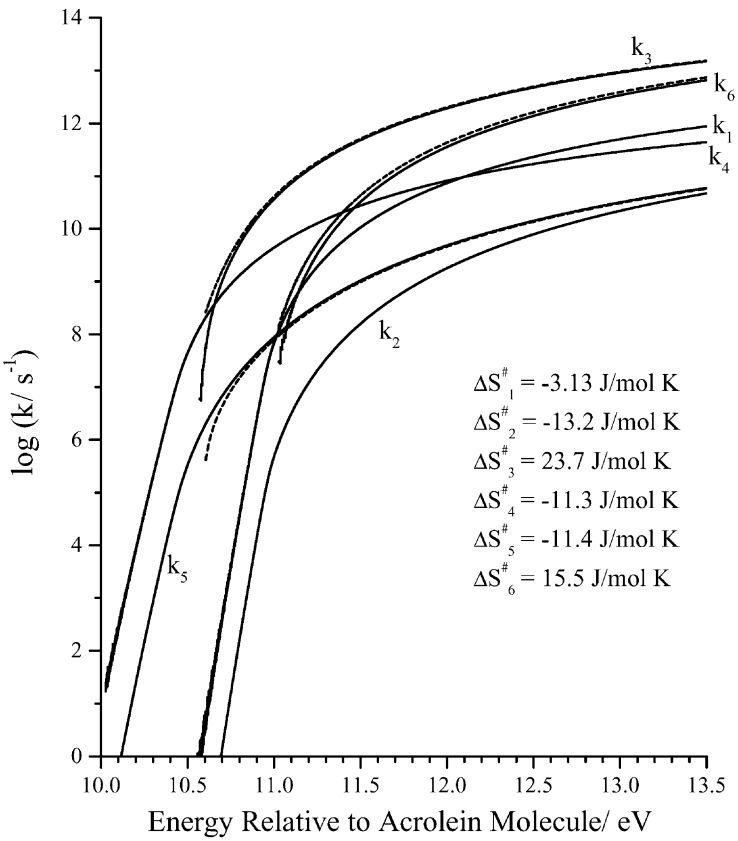

Fig. 4. RRKM calculated rate curves (solid lines) and the activation entropies (at 600 K) of all reactions. The k_{fast}, k_{med} and k_{slow} rate curves are indicated by dashed lines. Below 11.0 eV, k_{slow} follows k_1, whereas above 11.0 eV, it follows k_5.

these two reactions are simple bond-cleavage reactions. Fig. 4 also shows the k_{fast}, k_{med} and k_{slow} rate curves (dashed lines), which are complicated functions of k_1 to k_6. These three rate constants, given by the roots of Eq. (3), arise from the three potential energy wells. Their contributions to the total dissociation rate are directly proportional to the population of the three isomers during the course of reaction. It can be seen that at the energies above 11.0 eV, the k_{slow} curve is dominantly caused by the k_5 curve, which corresponds to the isomerization from C back to B. However, at this energy, k_{slow} is already greater than $10^8\ s^{-1}$. Below 11.0 eV, the energy region in which we observe a slow rate, k_{slow}, k_{med}, and k_{fast} correspond primarily to k_1, k_5, and k_3, respectively. Because the B and C wells in Fig. 3 are barely populated, the major contribution to the $C_2H_4^{\bullet+}$ formation is from k_1. The apparent "two-component" decay is thus caused by a combination of the acrolein molecule thermal energy distribution that extends over 0.15 eV, and the rapidly rising tunneling rate constants (10^4–$10^7\ s^{-1}$) over this small energy range. That is, the slow component is determined by the low energy ions, while the fast component is caused by the high energy tail of the thermal distribution.

Fig. 5 shows the population of A, B, C, P_1, and P_2 as a function of time at a photon energy of 10.98 eV over a time scale from 10^{-14} to 10^{-2} s. The acrolein thermal energy distribution and the instrument resolution are included in the ion energy. The vertical line at 5.6 μs corresponds to the time at which the parent ion leaves the acceleration region. The branching ratios for the product ions in the breakdown diagram of Fig. 2 are determined by the ion concentrations at that particular time. Ions decaying between 0.1 and 5.6 μs will appear as product ions in the TOF spectrum of

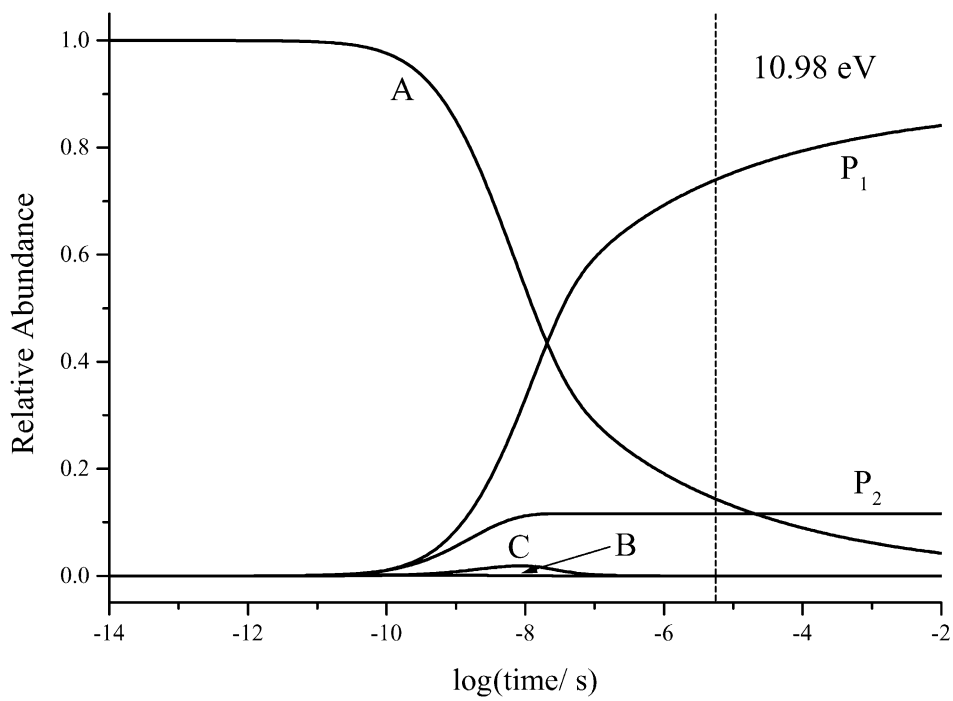

Fig. 5. Concentrations of the reactant, intermediates and products as a function of reaction time at the photon energy of 10.98 eV. The ion energy includes the photon energy of 10.98 eV, as well as the thermal energy distribution and the electron energy analyzer function. The dashed line indicates the time that it takes for the acrolein ion to traverse the first acceleration region. The breakdown diagram ion signal ratios at 10.98 eV correspond to the ion concentrations at this dashed line.

Fig. 1 between 12.5 and 15 μs. The production of the $C_3H_3O^+$ ion (P_2) levels off after 10^{-8} s because the $H^\bullet$ loss channel is associated only with a fast reaction. On the other hand, the lower energy ions associated with hot electrons produce only the $C_2H_4^{\bullet+}$ + CO products. It is evident in Fig. 5 that the intermediate ion, B is formed only sparingly, and the production of C is imperceptibly small. This is similar with the collision-induced dissociation result obtained by Traeger et al. [13] who suggested on the basis of the translational energies released that the distonic ion, B, did not isomerize to the other ions prior to decomposition. C is not produced because k_3 rises rapidly with internal energy relative to k_4 so that the dissociation reaction dominates over the isomerization to C. The small concentration of isomer B is determined by the ratio of k_1 and k_3. Isomers B and C are formed in even smaller concentrations at lower energies.

4.3. The thermochemical data

The 298 and 0 K thermochemical data of all relevant molecules and ions of this study are listed in Table 2, which also lists other available experimental or theoretical results of the 298 K heats of formation. The fitting of the data yielded energies for the $C_3H_3O^+ + H^\bullet$ dissociation energy and the TS_{AB}. Although the best known values in the potential energy

Table 2
Thermochemical data (kJ/mol)[a]

Species	$\Delta_f H^\circ_{298\,K}$	$\Delta_f H^\circ_{0\,K}$	$H^\circ_{298\,K} - H^\circ_{0\,K}$	Other results of $\Delta_f H^\circ_{298\,K}$
$C_3H_4O^{\bullet+}$ (A)	907 ± 10[b]	917 ± 10[c]	14.06[d]	916.3[e], 900[f], 904[g]
C_3H_4O (A)	−69 ± 10[b]	−58 ± 10[c]	13.91[d]	−67.6[e], −72[g], −66[h]
$C_3H_4O^{\bullet+}$ (B)	857 ± 20[g]	866 ± 20[g]	15.23[d]	843.5[e]
$C_3H_4O^{\bullet+}$ (C)	790 ± 10[g]	799 ± 10[g]	15.18[d]	797[e], 763[f], 797[i], 759[j], 778.7[k], 765 ± 5[l], 783.5 ± 0.3[m], 795[n]
$C_3H_3O^+$	<783 ± 10[o]	<790 ± 10[p]	13.33[d]	779[g], 751[j], 755.9[k], 749 ± 5[q]
$C_2H_4^{\bullet+}$	1067.24[o]	1075.365[r]	10.912[d]	–
CO	−110.53 ± 0.17[s]	−113.82 ± 0.17[c]	8.677[d]	–
$H^\bullet$	217.998 ± 0.006[s]	216.035 ± 0.006[c]	6.197[t]	–

[a] In the $H^\circ_{298\,K} - H^\circ_{0\,K}$ calculations, the heat capacity of electron was treated as 0.0 kJ/mol at all temperatures (the ion convention [37]). In order to convert to the electron convention, which treats the electron as a real particle, 6.197 kJ/mol should be added to the 298 K heat of formation of each ion.
[b] The average of three theoretical results.
[c] $\Delta H^\circ_{298\,K} \rightarrow \Delta H^\circ_{0\,K}$.
[d] Determined from DFT calculated vibrational frequencies.
[e] G2 result by McKee and Radom [29].
[f] Bouchoux and Hoppilliard [38].
[g] DFT results by Li and Baer [16].
[h] Allinger et al. [30]
[i] Scott and Radom [36].
[j] GIANT results by Lias et al. [39].
[k] Traeger et al. [13].
[l] Aubry et al. [40].
[m] Traeger [35].
[n] Nguyen and Nguyen [41].
[o] $\Delta H^\circ_{0\,K} \rightarrow \Delta H^\circ_{298\,K}$.
[p] Based on measured AE.
[q] Holmes et al. [42].
[r] $\Delta H^\circ_{0\,K}(C_2H_4)$ + IE, in which $\Delta H^\circ_{0\,K}(C_2H_4)$ is obtained by $\Delta H^\circ_{298\,K} \rightarrow \Delta H^\circ_{0\,K}$, and IE is 10.5138 ± 0.0006 eV [34], and $\Delta H^\circ_{298\,K}(C_2H_4) = 52.467$ kJ/mol [43].
[s] NIST Webbook [34].
[t] Wagman et al. [44].

surface of Fig. 3 is the $C_2H_4^{\bullet+}$ + CO dissociation limit, its energy could not be used to anchor the energy scale because the large barrier for the formation of the distonic ion, TS_{AB}, prevents product formation at its thermochemical limit. Instead, we are forced to anchor the scale with the neutral acrolein. There are no reliable experimental values for the heat of formation of the acrolein molecule. The value listed in the GIANT book of Lias et al. [39] is only an estimated value. On the other hand, there are three recent and independent theoretical values for the acrolein molecule heat of formation that agree quite well. These are based on a G2 calculation of McKee and Radom (−67.6 kJ/mol) [29], an MM3 molecular mechanics value of Allinger (−66 kJ/mol) [30], and a DFT value reported in the accompanying paper (−72 kJ/mol) [16]. Thus, we suggest a value of −69 ± 10 kJ/mol for the heat of formation of acrolein. This heat of formation combined with the $C_3H_3O^+$ appearance energy of 11.03 eV (0 K value) results in a 298 K heat of formation for $C_3H_3O^+$ of 783 ± 10 kJ/mol. Although this value is consistent with the DFT results [16], it is about 30 kJ/mol higher than the value suggested by Lias et al. [39] and the results obtained from two independent appearance energy measurements [13,42]. Traeger et al. [13] measured the appearance energy of the $C_3H_3O^+$ ion by dissociative photoionization of cyclopentanone. The problem here is that the first dissociation limit leads to $C_3H_4O^{\bullet+}$ (methylketene) + C_2H_4 at 10.42 eV. The dissociation to $C_3H_3O^+ + C_2H_5^{\bullet}$ has a weak onset at 10.85 eV. The weak onset could be due to collision-induced dissociation, or it could be due to the kinetic shift relative to the major dissociation limit to the methylketene ion. If it is the former, then the reported onset is too low (in agreement with our findings). But if it is due to a competitive shift, then the onset should if anything be lower still. The other determination by Holmes et al. [42] is based on an energy selected electron impact dissociative ionization onset ($C_3H_3O^+ + CH_3^{\bullet}$) from the methyl vinyl ketone precursor. The problem here is that methyl vinyl ketone does not have an experimentally known heat of formation, and thus, the derived $C_3H_3O^+$ energy is based on a Benson's additivity scheme for methyl vinyl ketone. The problem with our measurement is that $H^{\bullet}$ loss reactions are often accompanied by a reverse activation barrier [45] caused by, if nothing else, a centrifugal barrier due to the low moment of inertia of the departing H atom. Thus, our onset is strictly speaking only an upper limit, which could accommodate lower values for the $C_3H_3O^+$ energy. As pointed out in the theoretical paper on acrolein [16], TS_{13}, seems to have a structure that qualifies as a barrier for the $H^{\bullet}$ loss reaction. However, arguing against such a barrier is the fact that the experimental entropy of activation for the $H^{\bullet}$ loss step is +15.5 J/mol K. This moderately loose transition state is clearly associated with a dissociation step, rather than an isomerization step. Thus, we can offer no definitive conclusion concerning the $C_3H_3O^+$ heat of formation.

5. Conclusions

The dissociation dynamics and thermochemistry of acrolein are investigated using the threshold photoelectron–photoion coincidence spectroscopy. The breakdown diagram and time-of-flight distributions of the fragment ions associated with the lowest two dissociation channels, $C_2H_4^{\bullet+}$ + CO and $C_3H_3O^+ + H^{\bullet}$, are obtained. The $C_2H_4^{\bullet+}$ ion time-of-flight distributions appear multi-component with slow and fast rate constants. A three-well-two-channel model is suggested to describe the dissociation–isomerization reactions of the acrolein ion. The slow component of the reaction rate for $C_2H_4^{\bullet+}$ production is predominantly caused by a slow tunneling through the isomerization barrier between the acrolein and the intermediate distonic ion, $^{\bullet}CH_2CH_2CO^+$. The multi-component rates are a result of the thermal energy distribution that leads to a broad range of tunneling rate constants. The third and most stable ion, methylketene plays very little role in the reaction. Using derived energy barrier heights and an acrolein heat of formation of −69 ± 10 kJ/mol, an upper limit for the 298 K heats of formation of ionic CH_2CHCO^+ is found to be 783 ± 10 kJ/mol.

References

[1] C.B. Moore, J.C. Weisshaar, Ann. Rev. Phys. Chem. 34 (1983) 525.
[2] B.M. Hass, T.K. Minton, P. Felder, J.R. Huber, J. Phys. Chem. 95 (1991) 5149.
[3] W.H. Fang, J. Am. Chem. Soc. 121 (1999) 8376.
[4] H. Bock, S. Mohmand, T. Hirabayashi, A. Semkow, Chem. Ber. 115 (1982) 1339.
[5] A. Katrib, J.W. Rabalais, J. Phys. Chem. 77 (1973) 2358.
[6] P. Masclet, G. Mouvier, J. Electron Spectrosc. Relat. Phenom. 14 (1978) 77.
[7] H.V. Dam, A. Oskam, J. Electron Spectrosc. Relat. Phenom. 13 (1978) 273.
[8] W.V. Niessen, G. Bieri, L. Asbrink, J. Electron Spectrosc. Relat. Phenom. 21 (1980) 175.
[9] R.I. Reed, M.B. Thornley, Trans. Faraday Soc. 54 (1958) 949.
[10] M.A. Haney, J.L. Franklin, J. Chem. Soc., Faraday Trans. 65 (1969) 1794.
[11] T.W. Shannon, A.G. Harrison, Can. J. Chem. 39 (1961) 1392.
[12] A. Maquestiau, R. Flammang, P. Pauwels, Org. Mass Spectrom. 18 (1983) 547.
[13] J.C. Traeger, C.E. Hudson, D.J. McAdoo, Org. Mass Spectrom. 24 (1989) 230.
[14] F. Turecek, D.E. Drinkwater, F.W. McLafferty, J. Am. Chem. Soc. 113 (1991) 5958.
[15] F. Turecek, D.E. Drinkwater, F.W. McLafferty, J. Am. Chem. Soc. 113 (1991) 5950.
[16] Y. Li, T. Baer, Int. J. Mass Spectrom. 218 (2002) 19.
[17] T. Baer, J.A. Booze, K.M. Weitzel, in: C.Y. Ng (Ed.), Vacuum Ultraviolet Photoionization and Photodissociation of Molecules and Clusters, World Scientific, Singapore, 1991, pp. 259–298.
[18] J.W. Keister, T. Baer, M. Evans, C.Y. Ng, C.W. Hsu, J. Phys. Chem. 101 (1997) 1866.
[19] T. Baer, Y. Li, Int. J. Mass Spectrom., in press.
[20] M.J. Frisch, G.W. Trucks, H.B. Schlegel, G.E. Scuseria, M.A. Robb, J.R. Cheeseman, V.G. Zakrzewski, J.A. Montgomery, R.E. Stratmann, J.C. Burant, S. Dapprich, J.M. Millam, A.D. Daniels, K.N. Kudin, M.C. Strain, Ö. Farkas, J. Tomasi, V. Barone, M. Cossi, R. Cammi, B. Mennucci, C. Pomelli, C. Adamo, S. Clifford, J. Ochterski, G.A. Petersson, P.Y. Ayala, Q. Cui, K. Morokuma, D.K. Malick, A.D. Rabuck, K. Raghavachari, J.B. Foresman, J. Cioslowski, J.V. Ortiz, A.G. Baboul, B.B. Stefanov, G. Liu, A. Liashenko, P. Piskorz, I. Komáromi, R. Gomperts, R.L. Martin, D.J. Fox, T. Keith, M.A. Al-Laham, C.Y. Peng, A. Nanayakkara, C. Gonzalez, M. Challacombe, P.M.W. Gill, B.G. Johnson, W. Chen, M.W. Wong, J.L. Andres, M. Head-Gordon, E.S. Replogle, J.A. Pople, GAUSSIAN 98, Revision A.7, 1998, Gaussian, Inc., Pittsburgh, PA.
[21] C. Peng, H.B. Schlegel, Isr. J. Chem. 33 (1994) 449.
[22] C. Peng, P.Y. Ayala, H.B. Schlegel, M.J. Frisch, J. Comp. Chem. 17 (1996) 49.
[23] B. Sztaray, T. Baer, J. Am. Chem. Soc. 122 (2000) 9219.
[24] T. Baer, W.L. Hase, Unimolecular Reaction Dynamics: Theory and Experiments, Oxford University Press, New York, 1996.
[25] L.M. Duffy, J.W. Keister, T. Baer, J. Phys. Chem. 99 (1995) 17862.
[26] O.A. Mazyar, T. Baer, J. Phys. Chem. A 103 (1999) 1221.
[27] O.A. Mazyar, T. Baer, J. Phys. Chem. A 102 (1998) 1682.
[28] O.A. Mazyar, P.M. Mayer, T. Baer, Int. J. Mass Spectrom. Ion. Proc. 167/168 (1997) 389.
[29] M.L. McKee, L. Radom, Org. Mass Spectrom. 28 (1993) 1238.
[30] N.L. Allinger, S. Rodriguez, K. Chen, J. Mol. Struct. (Theochem.) 260 (1992) 161.
[31] J.W. Keister, T. Baer, R. Thissen, C. Alcaraz, O. Dutuit, H. Audier, V. Troude, J. Phys. Chem. A 102 (1998) 1090.
[32] W.H. Miller, J. Am. Chem. Soc. 101 (1979) 6810.
[33] T. Beyer, D.R. Swinehart, Commun. ACM 16 (1973) 379.
[34] http://webbook.nist.gov/chemistry/om/ 2000.
[35] J.C. Traeger, Int. J. Mass Spectrom. 194 (2000) 261.
[36] A.P. Scott, L. Radom, Int. J. Mass Spectrom. Ion. Proc. 160 (1997) 73.
[37] H.M. Rosenstock, K. Draxl, B.W. Steiner, J.T. Herron, Energetics of Gaseous Ions, J. Phys. Chem. Ref. Data, Vol. 6, American Chemical Society, Washington, DC, 1977.
[38] G. Bouchoux, Y. Hoppilliard, Can. J. Chem. 60 (1982) 2107.
[39] S.G. Lias, J.E. Bartmess, J.F. Liebman, J.L. Holmes, R.D. Levin, W.G. Mallard, Gas Phase Ion and Neutral Thermochemistry, J. Phys. Chem. Ref. Data, Vol. 17, Suppl. 1, NSRDS, US Government Printing Office, Washington, DC, 1988.
[40] C. Aubry, J.L. Holmes, J.K. Terlouw, J. Phys. Chem. A 101 (1997) 5958.
[41] M.T. Nguyen, H.M.T. Nguyen, Chem. Phys. Lett. 300 (1999) 346.
[42] J.L. Holmes, J.K. Terlouw, P.C. Bergers, Org. Mass Spectrom. 15 (1980) 140.
[43] M.W. Chase, NIST-JANAF Thermochemical Tables, American Institute of Physics, New York, 1998.
[44] D.D. Wagman, W.H.E. Evans, V.B. Parker, R.H. Schum, I. Halow, S.M. Mailey, K.L. Churney, R.L. Nuttall, The NBS Tables of Chemical Thermodynamic Properties, J. Phys. Chem. Ref. Data, Vol. 11, Suppl. 2, NSRDS, U.S. Government Printing Office, Washington, 1982.
[45] J.A. Booze, T. Baer, J. Phys. Chem. 96 (1992) 5715.